



# Insights into strain change of calcite by imaging defect-driven dissolution in the presence of $\text{Pb}^{2+}$



Ana F. Suzana <sup>1</sup>✉, Sang Soo Lee <sup>1</sup>, Irene Calvo-Almazán <sup>2</sup>, Wonsuk Cha <sup>3</sup>, Ross Harder <sup>3</sup> & Paul Fenter <sup>1</sup>

The presence of microscopic strain can determine the macroscopic properties of crystalline structures. However, the capability of quantifying and imaging strain variations in particles undergoing chemical reactions remains limited. Here, we exploit the ability of three-dimensional (3D) Bragg Coherent Diffraction Imaging (BCDI) to capture changes in the 3D strain maps and morphology of individual calcite (calcium carbonate,  $\text{CaCO}_3$ ) particles before and after dissolution in a lead-containing aqueous solution at pH 3.7. BCDI reconstructions show that calcite dissolution occurs preferentially at tensile-strained regions near macrosteps. This observation demonstrates that the local reactivity of calcite (i.e., as measured by the spatial distribution of its dissolution rate) is influenced by pre-existing strains for as-grown calcite nanocrystals. Additional studies will be required to develop a predictive understanding of the strain–reactivity relationship.

Calcium carbonate ( $\text{CaCO}_3$ ), one of the most abundant minerals on Earth, occurs naturally in three anhydrous polymorphs: vaterite, aragonite, and calcite, with calcite being the most thermodynamically stable phase<sup>1</sup>. Carbonate minerals play a critical role in buffering natural waters, serving as nutrient sources, and acting as sinks for heavy metal contaminants<sup>2,3</sup>. Such processes directly influence the biogeochemical cycling and transport of elements in aquatic and terrestrial systems. Therefore, a detailed understanding of the stability and reactivity of calcite and calcite–metal interactions is essential for elucidating the mechanisms governing metal mobility and retention in the environment, the global carbon cycle, and the development of more efficient water purification technologies<sup>4,5</sup>.

The coupling between large-scale geochemical processes and nanoscale mechanisms is mediated by the fundamental reactivity of mineral surfaces. At the macroscale, calcite dissolution and precipitation influence the mobility of metals and the cycling of carbon in natural systems. However, these processes are ultimately governed by nanoscale interactions at the mineral–solution interface, where atomic-scale strain, surface topography, and ion transport dictate reaction kinetics. Understanding how nanoscale strain and dissolution dynamics influence macroscale processes is therefore critical for linking molecular mechanisms to environmental phenomena.

The fundamental mechanisms driving calcite reactivity have been extensively investigated using operando experimental methods such as atomic force microscopy (AFM)<sup>6</sup> and X-ray reflectivity (XR)<sup>7</sup>. These studies often utilize model systems such as single-crystalline materials reacting with

large solution volumes to maintain nominally stable chemical conditions, such as pH and dissolved metal ion concentrations<sup>7–10</sup>. While these approaches are capable of capturing the reactivity of carbonate surfaces at the nanoscale, the inherent complexity of carbonate systems presents significant challenges to their application. Localized variations in solution chemistry, driven by dynamic dissolution and (re)precipitation of carbonate minerals, create concentration gradients near the mineral–solution interface that control the diffusivity of ions, solution pH, and, consequently, reactivity. Under diffusion-controlled conditions, the rates and mechanisms of carbonate growth and dissolution reactions become increasingly complex, as the transport of ions or molecules to and from specific surface features, such as terraces and steps, governs reaction kinetics.

The presence of dissolved heavy metals ions, such as  $\text{Pb}^{2+}$ , can profoundly influence the dissolution and growth dynamics of calcite; however, its role is not well-understood mechanistically<sup>3,11</sup>. These ions may adsorb onto the mineral surface, modify surface energy, or interfere with the transport of reactants and products, thereby altering reaction rates and mechanisms. For example, the interaction of divalent toxic metals like  $\text{Pb}^{2+}$  and  $\text{Cd}^{2+}$  with calcite have been extensively studied in recent decades<sup>12–16</sup> due to their occurrence in natural systems and the consequent environmental toxicity associated with them. The larger ionic radius of  $\text{Pb}^{2+}$  compared to  $\text{Ca}^{2+}$  makes it incompatible with the calcite crystalline structure and several studies have reported limited  $\text{Pb}^{2+}$  incorporation into the calcite lattice<sup>12,15</sup>. Understanding the mechanisms of calcite dissolution in the presence of

<sup>1</sup>Chemical Sciences and Engineering Division, Argonne National Laboratory, Lemont, IL, 60439, USA. <sup>2</sup>Institute of Nanosciences and Materials of Aragon (INMA) – University of Zaragoza, Zaragoza, Spain. <sup>3</sup>Advanced Photon Source, Argonne National Laboratory, Lemont, IL, 60439, USA. ✉e-mail: [asuzana@anl.gov](mailto:asuzana@anl.gov)

dissolved metals remains challenging because the interactions between metal ions and calcite surfaces involve complex, competing processes such as adsorption, incorporation into the crystal lattice, and surface precipitation. Carbonate surface reactivity is also influenced by solution chemistry, pH, and temperature. Recent studies have demonstrated that calcite surfaces exposed to Pb-containing undersaturated solutions undergo complex morphological changes<sup>17–19</sup>. These include alterations in the shape of calcite microcrystals, the development of intricate surface topographies, including rhombic pyramids, and the precipitation of secondary lead carbonate phases. Such findings highlight the complex interplay between calcite reactivity and dissolved metal ions, emphasizing the need for advanced analytical techniques to unravel these processes in natural and synthetic systems.

An unexplored aspect of the interactions of these heavy metal ions with carbonate surfaces is their role in influencing lattice strain during reactions. The incorporation of these ions is expected to induce strain within the calcite crystalline structure as a result of differences in ionic radii. In this scenario, a knowledge gap persists due to the limited availability of techniques sensitive to both 3D morphology and lattice defects. Here, we use Bragg Coherent Diffraction Imaging (BCDI, see Supplementary Information) to visualize in 3D the active sites of the calcite dissolution reaction in the presence of Pb<sup>2+</sup> and uncover the changes in the strain state in the evolution of particle morphology. This study demonstrates the application of BCDI in mineral dissolution, providing an additional tool to complement established surface-specific techniques such as scanning electron microscopy (SEM) and AFM. BCDI reconstructions revealed that the calcite particles investigated here exhibit macrosteps on their surfaces, which are characterized by tensile strain. Furthermore, regions surrounding these macrosteps display preferential dissolution, suggesting that the macrosteps likely function as active sites for dissolution in the presence of Pb<sup>2+</sup>. X-ray reflectivity data showed Pb<sup>2+</sup> incorporation into the calcite crystalline structure, suggesting that the complex dissolution behavior may be linked to the incorporation of Pb<sup>2+</sup>, while BCDI and SEM imaging revealed the formation of holes on the calcite surface following the reaction. The reconstructed BCDI images, having sub-Ångström sensitivity to 3D lattice distortions, show the power of BCDI microscopy as a tool for probing strain states in 3D, offering insights into the strain distribution not accessible with other techniques and structural transformations occurring at the atomic scale.

## Results

### Morphology and phase of calcium carbonate

The methodology for calcite synthesis follows refs. 20–22 with modifications<sup>23</sup> and consists in growing the calcite crystals on gold thin films functionalized with self-assembled monolayers (SAMs) with calcium

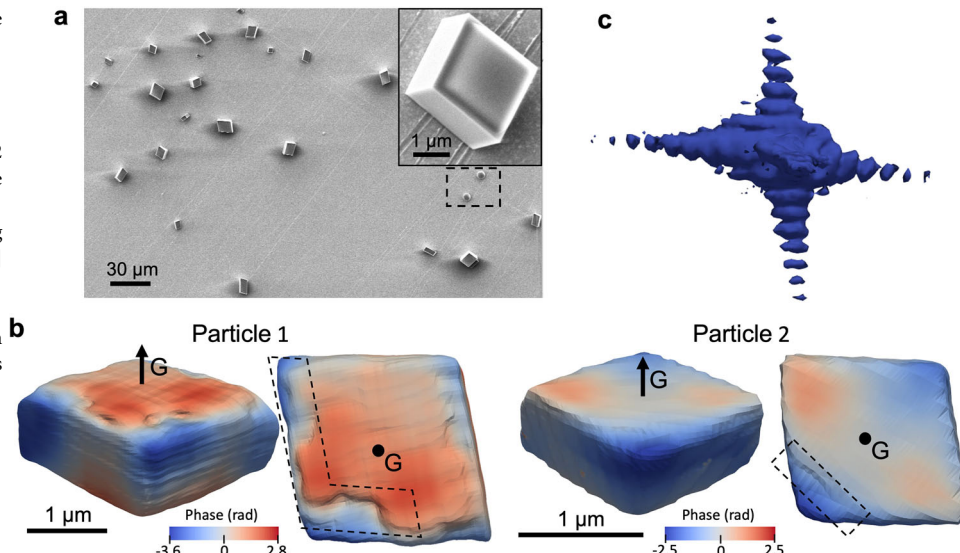
chloride and ammonium bicarbonate as precursors (see Methods below for detailed information). Figure 1a shows a representative SEM image of the distribution of calcite crystals, with an inset that displays a magnified view of a single ~2.4 μm crystal. The typical rhombohedral calcite crystals are easily identified, along with spherical particles which are presumably vaterite (see the region within a dashed rectangle) appearing as a minority phase. Since BCDI is limited by the beam size to image single crystals in the 1–2 μm range, this study is centered around crystals like the one displayed in Fig. 1a inset.

### Local distortion mapping of calcite single crystals in pristine state

While powder X-ray diffraction (XRD) reveals the average crystalline structure and particle size in a sample consisting of a large number of particles, BCDI measures the structure of individual crystals, including the particle shape and the internal displacement field with sub-Ångström sensitivity. This is achieved by measuring the 3D intensity distributed around a specific Bragg peak using a so-called rocking curve scan. It consists in coherently illuminating the sample at various orientations within a narrow angular window (~1 degree) around the corresponding Bragg angle and recording 2D images of the diffraction pattern at each orientation. The measured 3D Bragg intensities are the main input for phase retrieval algorithms (see Methods), which, by inversion, provide a complex valued map of the crystal where the amplitude corresponds to the electron density and the phase can be related to the lattice displacement field projected onto the measured Bragg peak. Nano- and micro-particles can exhibit differences from the bulk crystal structure due to their surface properties and morphology. Surface defects can induce lattice strains, which may propagate into the entire particle. BCDI enables direct visualization of a particle's strain and morphology, providing a valuable insight into how lattice strains influence chemical reactivity.

The 3D BCDI reconstruction of two pristine (i.e., as-grown) calcite crystals measured under ambient conditions is presented in both side and top views in Fig. 1b. These crystals are referred to as “Particle 1” and “Particle 2” hereafter (the pristine structure of Particle 2 has been published elsewhere<sup>23</sup>). The 3D particle electron density is shown as an isosurface. Internal displacement fields are indicated with a color map, where red and blue denote positive and negative atomic displacements, respectively. These displacements are projected along the [104] direction, which corresponds to the G vector (represented by black arrows) measured during the experiment. Details of the BCDI measurement are described in the Methods section. Figure 1c displays the 3D Bragg peak of Particle 1 in its pristine state. The sharp fringes in three directions show that the oversampling ratio criteria is met<sup>24</sup>. The shape of the crystals is in excellent agreement with the

**Fig. 1 | SEM and BCDI results.** **a** SEM image of the calcite crystals synthesized on the gold thin film covered with SAMs. The inset shows an individual calcite particle, and the dashed line rectangle highlights vaterite particles. **b** Side and top views of the reconstructions from BCDI data for Particles 1 and 2 (in their pristine states) shown as an isosurface. The color map corresponds to the phase, which is the projection of the lattice displacement field  $u(r)$  along the G-vector (indicated by black arrows) in the [104] direction:  $\phi(r) = G_{HKL} \cdot u(r)$ <sup>25</sup>. The dashed boxes highlight macrosteps observed on the top calcite surfaces. The phases shown for Particle 1 have been unwrapped<sup>27</sup>. **c** 3D diffraction peak of Particle 1 in its pristine state measured in a rocking curve scan.



rhombohedral calcite crystal shape observed in the SEM images (Fig. 1a). The crystal dimensions,  $2.3 \times 2.4 \times 1.4$  (height)  $\mu\text{m}^3$  for Particle 1 and  $1.3 \times 1.3 \times 0.8$  (height)  $\mu\text{m}^3$  for Particle 2, are also similar to those seen in the inset of Fig. 1a. Notably, the top facets of the reconstructed particles have macrosteps, which are highlighted by the black dashed lines (Fig. 1b). Similar features were seen in SEM images of particles grown from different batches using the same growth conditions (Supplementary Fig. S1).

Particle 1 exhibits significant phase variations in certain regions, indicating that the displacement field is highly pronounced even in its pristine state, as previously described<sup>20</sup>. This is evident in the original wrapped reconstruction where the color changes suddenly from blue to red (Supplementary Fig. S2). These abrupt color changes correspond to phase shifts of  $2\pi$  radians, where the total projected lattice displacements become greater than the 104-layer spacing ( $d = 3.035 \text{ \AA}$ )<sup>25</sup>.

### Dissolution of calcite in acidic $\text{Pb}^{2+}$ -containing solutions

After recording the 3D Bragg peak of the pristine crystals, the sample was exposed to  $\sim 100 \mu\text{L}$  of an acidic  $\text{Pb}^{2+}$  solution, having  $[\text{Pb}^{2+}] = 5 \text{ mM}$  and  $\text{pH} = 3.7$ , for 10 min. Following the reaction, the excess solution was carefully removed using absorbent paper and subsequently dried with a stream of air. The sample was then left to air-dry for  $\sim 10$  min (refer to the Methods section for further details). New 3D diffraction data were then acquired using the same method as for the pristine particles.

The 3D BCDI reconstructions for the pristine (Fig. 2a, c) and reacted (Fig. 2b, d) states are compared for Particles 1 and 2, respectively. In each case (Fig. 2b, d), the structure of the reacted particle is shown along with that of the pristine state (plotted as a semitransparent isosurface). The color map represents the strain (from  $-0.05$  to  $0.03\%$  for Particle 1, and from  $-0.015$  to  $0.015\%$  for Particle 2) along the [104] direction (see Methods for strain calculation details). The bottom of each panel displays slices taken at the position denoted by the yellow dashed lines in the upper 3D plots. Additionally, the contour of the cross-sections (black line) for the crystal reacted with the acidic  $\text{Pb}^{2+}$ -containing solution is shown in Fig. 2a, c. Three remarkable observations can be made when comparing the pristine and reacted states. First, there is preferential dissolution near the macrosteps for both particles, including the region near the upper part of the macrostep of Particle 1, as clearly seen in the cross-section plots. Second, positive (tensile) strain is very pronounced for the pristine state in the macrostep regions as highlighted by the solid black lines in the pristine 3D plots. Lastly, the formation of characteristic features similar to “holes” on the surface is seen for the reacted particles, as highlighted by the white arrows. There are evident connections between these three observations, as discussed next.

The holes on the surface of Particle 1 after the reaction indicate that this region contained numerous active sites for dissolution while the rest of the surface remains relatively flat. Interestingly, the pristine state presents very pronounced positive (i.e., tensile) strain close to this region (Fig. 2a, black arrow in the cross-section), indicating a connection between lattice strain and calcite reactivity. For Particle 2, the fastest dissolution is observed at the bottom left corner in the top view of Fig. 2c, d. This region corresponds to a macrostep present in the pristine state (highlighted by the black dashed rectangle in Fig. 1), with high tensile strain values, very similar to what has been seen for Particle 1. We interpret that the dissolution reaction front initiated in the regions near the macrosteps, as indicated by the yellow arrows in Fig. 2b. This interpretation is supported by the SEM images presented below, taken from the same calcite particles before and after dissolution reaction in the presence of  $\text{Pb}^{2+}$ . For both particles, the morphology of the crystal facet attached to the substrate remains relatively unaffected by reaction except near the corners where most dissolution is observed. The dissolution rate was calculated from the BCDI results taking into account that the volume loss was  $1.9 \times 10^9 \text{ nm}^3/\text{min}$  for Particle 1, while for Particle 2, the loss was  $2.7 \times 10^7 \text{ nm}^3/\text{min}$ . Considering the dimensions of each particle (see above), the reaction rate was calculated to be  $9.7 \times 10^{-6} \text{ mmol cm}^{-2} \text{ s}^{-1}$  for Particle 1 and  $4.5 \times 10^{-7} \text{ mmol cm}^{-2} \text{ s}^{-1}$  for Particle 2. These values are similar to those measured using digital holography

microscopy in a previous study<sup>3</sup>, which reported a dissolution rate of  $4.75 \times 10^{-7} \text{ mmol cm}^{-2} \text{ s}^{-1}$  in a pH 3.7 solution containing 5 mM of  $\text{Pb}^{2+}$ .

SEM analysis shows similarly complex morphologies in reacted calcite crystals. Figure 3a, b show SEM images of the same calcite particle before (pristine), and after 10 min of reaction with a  $\text{Pb}^{2+}$ -containing solution at pH 3.7. The reacted particle in Fig. 3a shows the formation of etch pits mostly in the right half of the particle and protrusions that are presumably the micropyramids reported in previous studies<sup>17–19</sup>. In addition, we observe the formation of a hole in the upper left part of the crystal. Remarkably, the SEM image of the pristine particle shows a slight contrast change in this region, as indicated by the white arrow, suggestive of a pre-existing defective structure. These observations are in excellent agreement with the BCDI results: defective (strained) regions seem to be correlated to the physical location of the active dissolution sites on the calcite surface. The particle shown in Fig. 3b has clear macrosteps on its lateral surface, as highlighted by the white dashed line rectangle. These features are similar to that seen on the top surface of both particles in the BCDI reconstructions, especially for Particle 1 (note that rounding of the steps in the BCDI reconstructions is likely due to the limited spatial resolution of the technique). After 10 min of reaction, the macrosteps (region highlighted by a white dashed line rectangle) dissolve, indicating that they are preferential reaction sites for dissolution.

To further clarify the role of defects in calcite dissolution, we conducted a separate SEM imaging experiment on a particle deliberately chosen for its numerous grain boundaries (Fig. 3c). The morphological change of this particle was imaged during reaction in a  $\text{Pb}^{2+}$ -free HCl solution at pH 3.7 for 1.5 h (see Method section for more details). After 30 min, pronounced dissolution is observed in the corners and grain boundaries, which have a higher number of undercoordinated ions. The presence of the grain boundaries also effectively increases the surface area, enhancing the particle's overall reactivity. The grain boundary highlighted by a white dashed rectangle in the image taken for the pristine state is found to be a dominant site for the dissolution after 1.5 h of reaction. After 1 h of reaction, a hole appears on a surface region between grain boundaries (white dashed line rectangle). In this case, there is a clear connection between the presence of defects in the form of grain boundaries and the most active reaction sites.

The BCDI reconstructions and the SEM images clearly indicate that dissolution reaction varies significantly across the particles, and that this appears to be correlated with the distribution of strain and defects in the particles. We can extend these observations by comparing the strain distributions across the particles before and after reaction. In Fig. 4, we compare the surface and bulk strain histogram plots for Particles 1 and 2. For this analysis, we define the “surface” as the regions within a depth of one voxel from the isosurface boundary that defines the external surface (the pixels have a size of 10–20 nm, depending on the reconstruction). The surface strain is measured within only those voxels. From our preliminary analysis, we found that the bottom surface of the crystal, which was in contact with the substrate, did not change significantly during reaction with the solution, and therefore was excluded from the analysis. In contrast, the “bulk” strain regards all the other voxels within the particles (i.e., the whole particle minus surface voxels). We first explore the similarities of the histogram plots of both particles and then highlight the differences between them.

A common characteristic of both particles is that the strain distribution is wider at the particle surface than in the bulk, in both pristine and reacted states. Also, the pristine particles show a significant number of surface voxels with very large strain. This is expected since, as highlighted before, the surface contains a high number of undercoordinated atoms with dangling bonds and likely has more pronounced strain. We observe that the strain at the particle surface changes significantly upon reaction, while the changes in the bulk strain distributions are smaller. Given that the strained regions near macrosteps appear to act as active sites for the dissolution reaction, this reaction has the effect of removing the most highly strained sites, and therefore strain relief might be expected. Notably, after the reaction, the compressive (negative) surface strain is relieved in both particles. We interpret this through two possible scenarios. First, regions of compressive

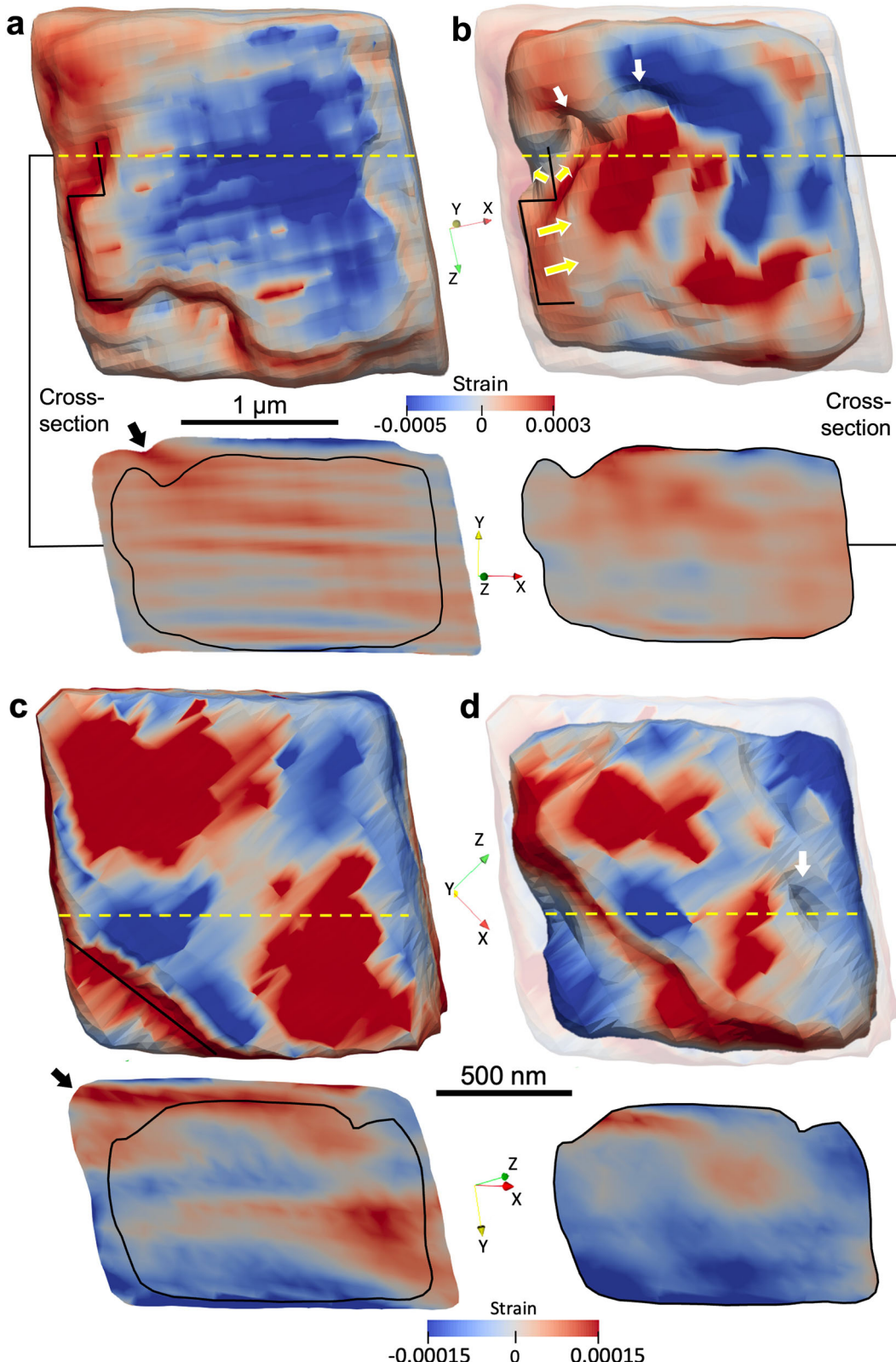


**Fig. 2 | BCDI reconstructions for Particles 1 and 2.** **a–d** 3D reconstructions (top) and cross-sections (bottom) taken in the yellow dashed line shown as strain for Particle 1 (**a, b**) and Particle 2 (**c, d**). **a, c** Plot of the pristine state, and (**b, d**) after 10 min of dissolution reaction in acidic  $\text{Pb}^{2+}$  solution. Note that the 3D reconstruction of the pristine state is also shown here (in **b, d**) as a semitransparent isosurface), and the contours of the cross-section for the reacted crystals are shown in (**a, c**). The black arrows in **a, c** indicate regions that are highly positively strained

and the yellow arrows in (**b**) indicate the direction to which the reaction front proceeded. The white arrows in (**b, d**) indicate holes on the calcite surface. The black lines in the 3D reconstructions in (**a–c**) highlight the macrosteps on the calcite surface. The 3D coordinates for each set of reconstruction are shown for the 3D and 2D plots.

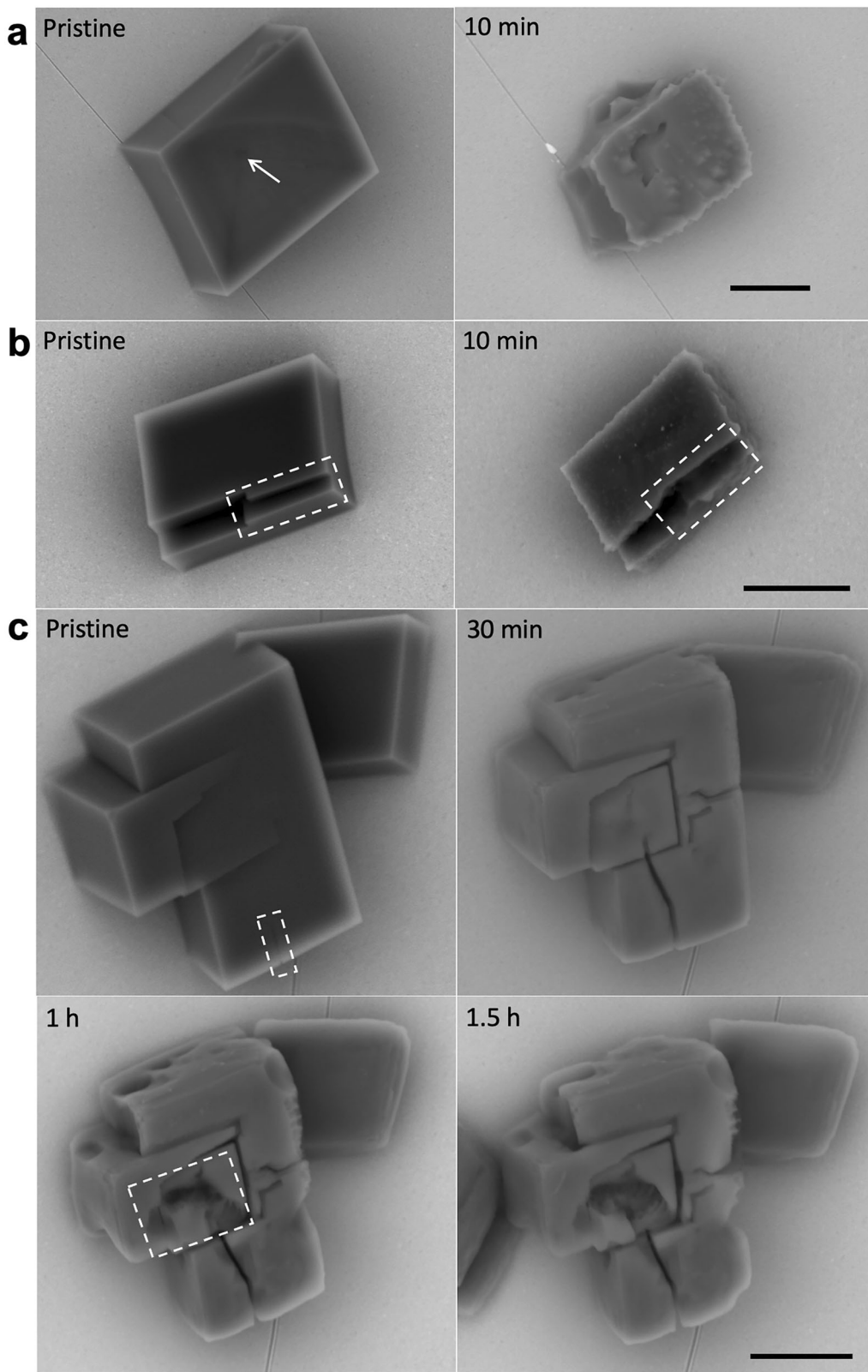


**Fig. 3 | SEM images of calcite before and after dissolution reaction.** **a, b** SEM images of calcite crystals synthesized using the ammonium diffusion approach in the pristine state, and after 10 min of reaction with a  $\text{Pb}^{2+}$ -containing solution at pH 3.7.

**c** SEM images of a calcite crystal having multiple grain boundaries before and after dissolution reaction in a Pb-free pH 3.7 solution (acidified with HCl). The scale bars represent 5  $\mu\text{m}$ . The same magnification is used for pristine and reacted states.

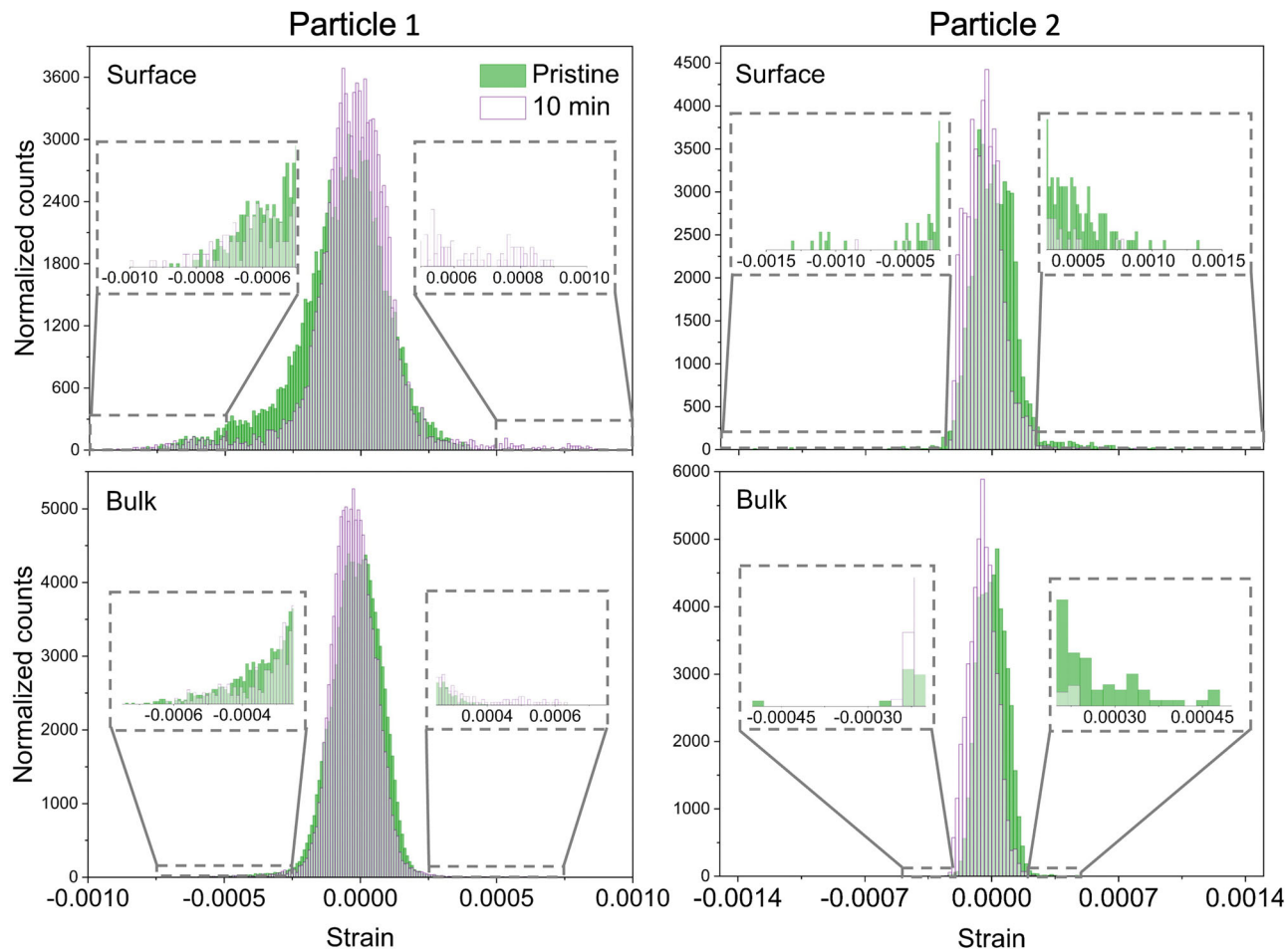


**Fig. 4 | Histogram plots of surface and bulk strain for Particles 1 and 2.** Green color represents the strain distributions in the pristine state, and purple contour represents the particles after reaction in a  $\text{Pb}^{2+}$ -containing solution for 10 min. The

top panels display the strain distribution for the surface voxels, and the bottom panels show the distribution for the bulk voxels. All histograms have been normalized (see Methods for details).

strain may serve as active sites for the reaction. Second, since Pb is known to incorporate into the calcite crystalline structure<sup>7,12,15</sup>, the relief of compressive strain could be coupled with Pb incorporation (see the next section for details on Pb incorporation into the calcite structure). Surprisingly, an opposite trend is seen regarding high values of tensile (positive) strain at the surfaces of the two particles: Particle 1 shows buildup of this type of strain, while Particle 2 displays a reduction. For the bulk voxels, there is a shift from a small tensile to a small compressive strain upon reaction that is observed for both particles. The complexity of this behavior suggests that it may arise from multiple causes, such as the intrinsic heterogeneities in these nano- and microparticles, coupled with the spatial variations in the active sites for the dissolution reactions. For example, the change in the sign of the bulk lattice strain upon reaction may suggest that the removal of most highly strained sites allows the particle strain to shift to accommodate the remaining residual strains, but more observations will be needed to establish the causal relationships between these factors.

#### Structural analysis of $\text{Pb}^{2+}$ incorporation in single crystal calcite from X-ray reflectivity data

The role of Pb in influencing the strain seen in the calcite particles is not resolved by BCDI images, but we hypothesize that it is related to the incorporation of Pb within the calcite surface. In this section, we analyze the behavior of isolated calcite surfaces using in-situ crystal truncation rod (CTR) measurements to understand how  $\text{Pb}^{2+}$  ions incorporate into and modify the calcite surface. Our analyses were performed on the (104) surface of a large calcite crystal (with a surface area of  $\sim 1 \times 1 \text{ cm}^2$ ) that was cleaved and immersed in a calcite saturated solution (CSS). The key difference

between XR and BCDI is that the spatial resolution of the CTR measurement can reach  $\sim 1 \text{ \AA}$  along the surface normal direction while the resulting structure is averaged within the surface plane<sup>26</sup>. In comparison, the spatial resolution is  $\sim 10\text{--}20 \text{ nm}$  in BCDI and is approximately isotropic<sup>20</sup>. The high resolution of CTR coupled with its surface sensitivity makes CTR an ideal probe to investigate interfacial processes. Previous work conducted by our group reported  $\text{Pb}^{2+}$  incorporation onto calcite<sup>7</sup>, with the main difference being that the measurement was performed by flowing a  $\text{Pb}^{2+}$ -containing solution. In contrast, the current work presents results for measurements conducted using a static reaction solution in contact with the calcite surface.

In-situ XR data of the calcite (104) interface in contact with CSS (black symbols), and with the acidic  $\text{Pb}^{2+}$  solution at pH 3.6 (blue symbols), are shown in Fig. 5a. The data were measured in the range of momentum transfer,  $Q$ , from  $0.44\text{--}6.84 \text{ \AA}^{-1}$ . (Here,  $Q \equiv (4\pi/\lambda) \sin(\theta)$ , where  $\lambda$  is the X-ray wavelength and  $\theta$  is the incident angle of the beam with respect to the surface plane). Both sets of data show the expected CTR shape associated with the tails of the Bragg peaks that are located at  $Q = 2.06, 4.14$ , and  $6.21 \text{ \AA}^{-1}$  and with weak reflectivity signals ( $R < 10\%$ ) associated with interfacial sensitivity. The remarkable difference between these data is the increase in reflectivity signal in “midzones”, regions between the Bragg peaks, for the  $\text{Pb}^{2+}$ -reacted sample, most notably near  $Q = 1.8$  and  $3.6 \text{ \AA}^{-1}$ , that is, slightly below those of the calcite (104) and (208) Bragg peaks, respectively (Fig. 5a). These shoulders of the Bragg peaks result from the formation of multilayer films that had an internal layer spacing larger than the calcite (104) lattice spacing. The calcite layer spacing can increase by incorporation of Pb ions since the ionic radius of  $\text{Pb}^{2+}$  (118 pm) is larger than that of  $\text{Ca}^{2+}$  (100 pm). Determination of structural changes to the calcite interfacial structure

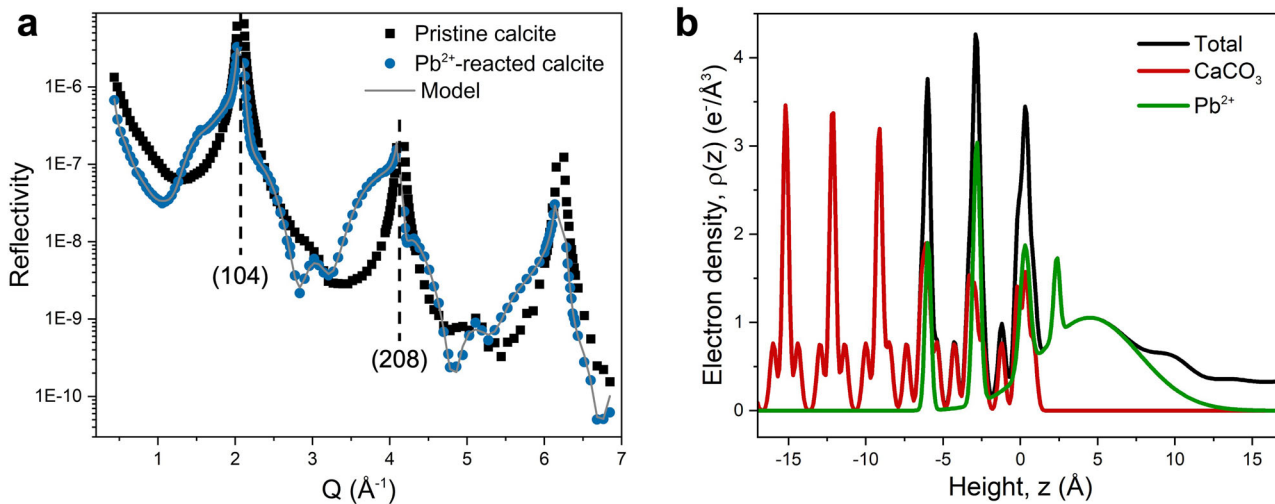


**Fig. 5 | XR data and modeling of pristine and  $\text{Pb}^{2+}$ -reacted calcite.** **a** XR data for the pristine calcite (104) surface in calcite saturated solution (CSS, black) and that reacted with a 50 mM  $\text{Pb}(\text{NO}_3)_2$  solution at pH 3.6 for 15 min (blue). The gray line is the calculated reflectivity from the optimized structural model. **b** Derived electron density profile as a function of height ( $z$ ) from the calcite surface corresponding to the best-fit model for the calcite surface reacted with Pb (the black line is the total

electron density of the reacted surface). The red line represents the density profile corresponding to  $\text{CaCO}_3$  for both the bulk lattice (shown for the layer at  $z = -15$ ) and for the distorted calcite surface, and the green line represents the  $\text{Pb}^{2+}$ -specific density profile (both those incorporated in the top three calcite layers and sorbed on the surface).

associated with the reaction with  $\text{Pb}^{2+}$  solutions (see Methods) was done using least-squares fitting techniques, described in the Supporting Information. The XR signals calculated from the best-fit model of the reacted calcite surface is shown (Fig. 5a, gray line). The model includes an interfacial layer in which the top six Ca and  $\text{CO}_3$  layers have a variable structure and composition and exhibits strong agreement with the experimental data.

Figure 5b displays the electron density profile derived from the best-fit model, with quality of fits,  $\chi^2 = 5.40$ , and R-factor = 0.051, for the sample reacted with acidic  $\text{Pb}^{2+}$  solution. The total electron-density profile as well as those of the sub-structures including the reacted calcite (labeled as  $\text{CaCO}_3$ ) and interfacial  $\text{Pb}$  species (labeled as  $\text{Pb}^{2+}$ ) are shown as a function of height ( $z$ ) measured from the crystallographic position of Ca in the topmost calcite unit-cell layer. The topmost layers of the calcite surface reveal significant enhancement in total electron density due to the incorporation of  $\text{Pb}^{2+}$ , similar to those reported in previous studies<sup>7,15</sup>. The best-fit model (Table S1) indicates that  $\text{Pb}^{2+}$  ions incorporate into the top three calcite unit-cell layers, spanning the total layer thickness of  $\sim 1 \text{ nm}$ . The broad peak indicated by green in Fig. 5b may correspond to the secondary  $\text{Pb}$  carbonate phases that precipitated on the calcite surface as seen previously<sup>7</sup>. The XR measurements were conducted in a static solution over an extended time ( $\sim 1 \text{ h}$ ) during which continuous dissolution of calcite would induce supersaturation of cerussite and hydrocerussite in the solution.

## Discussion

The study of calcite crystals provides valuable insights into their structural changes, particularly when they are exposed to acidic aqueous solutions containing  $\text{Pb}^{2+}$  ions. Through the application of BCDI, we have identified significant variations in strain when comparing the states prior to and after 10 min of dissolution in acidic solutions containing  $\text{Pb}^{2+}$ . Additionally, SEM has revealed notable morphological transformations occurring during the dissolution process within the time interval of 10 to 90 min. Based on these findings, we further explore the origins of crystallographic defects in pristine calcite particles and their impact on the carbonate reactivity under diffusion-controlled conditions, where reaction rates and mechanisms are governed by localized chemical variations around evolving surface features.

The pronounced strain observed in the pristine calcite particles (Fig. 2) is likely due to multiple factors. A key characteristic of calcium carbonate minerals, crucial for materials synthesis, is their polymorphism. Previous

investigations indicate that the calcite crystallization often involves intermediate phases, such as amorphous calcium carbonate (ACC) precursors and metastable vaterite, which transform into calcite through dissolution-reprecipitation processes<sup>27–31</sup>. Since vaterite is seen in the final sample, it is possible that these phase transformations happened during the synthesis. SEM images taken after 1 min of reaction to produce the calcite particles show aggregates composed of Ca-containing nanoparticles (Supplementary Fig. S3), which resemble the characteristics of ACC reported in these studies. In a previous investigation, the stabilization of ACC phases was reported on gold films functionalized with hydroxyl-terminated SAMs<sup>32</sup>, which is the case of the current work. Although the reaction mechanism was not fully investigated in this work, the residual distortion in the displacement field can come from a sequence of phase transformations during calcite crystal growth, specifically during dissolution-reprecipitation processes as described previously<sup>23</sup>. Another factor that can contribute to the displacements is lattice strain induced by growth on the SAMs. While this structural relationship is not likely to have a simple epitaxial explanation, previous results have shown that the interaction is sufficient to lead to the formation of dislocations in the calcite particle<sup>21</sup>. Indeed, the strain calculated for the bottom facet in contact with the SAMs of both particles is much more pronounced than the other facets, as shown in Supplementary Fig. S4. It is important to highlight that despite the fact that the displacement field is pronounced for the particles shown here, our previous study<sup>23</sup> showed that the crystalline structure is much more defective for calcite particles synthesized in far-from-equilibrium synthesis conditions, such as precipitation from supersaturated solutions.

Defects such as etch pits and grain boundaries are known to dissolve faster than defect-free regions. Although this relationship is well-described in literature, there is little information available on the effect of strain on dissolution of calcite crystals, especially when a foreign ion is present. Previous experimental works<sup>33,34</sup> on the role of strain in calcite dissolution kinetics found that the dissolution rate is enhanced for strained crystals compared to non-strained ones. A previous BCDI investigation<sup>20</sup> of calcite crystals during growth and dissolution cycles revealed that calcite facets with the highest number of surface dislocations grew faster, and the strain tended to be larger closer to the surface as compared to the center of the crystal, similar to what has been observed in the current work. Although the particles in our BCDI experiment were measured under nominally identical conditions, they exhibit different dissolution rates. Such particle-to-particle

variability is expected, because the density and distribution of active sites (e.g., macrosteps and regions under tensile strain) can vary substantially between crystals. As shown in Figs. 1 and 2, the two particles display distinct macrostep architectures and surface-strain landscapes—features known to modulate defect-mediated dissolution. Consistent with this view, the surface-strain histograms (Fig. 4) show a broader, heavier-tailed distribution for Particle 1, in line with its higher measured dissolution rate. Additionally, the local solution composition within the static droplet—including gradients in dissolved ion concentrations, pH, and the calcite saturation index—likely depends on extrinsic factors, such as particle density in the droplet. These factors can modulate the chemical driving force and thereby contribute to differences in dissolution rate.

The formation of complex morphologies on calcite surfaces after dissolution in  $\text{Pb}^{2+}$ -containing acidic aqueous solutions was detected by SEM, but it is unclear in the BCDI reconstructions. We attribute this observation to the presence of intrinsic heterogeneities in nano/micro particles, where variations in dissolution behavior occur from one particle to another. This can be illustrated by SEM images taken for the sample measured after the BCDI experiment. These images show the formation of holes on the surface of the particles, with no clear formation of micropyramids (Supplementary Fig. S5), in agreement with the BCDI reconstructions. Since the formation of the micropyramids is related to  $\text{Pb}^{2+}$  incorporation into the calcite crystalline structure<sup>3</sup>, the fact that there is no formation of micropyramids demonstrates that the amount of  $\text{Pb}^{2+}$  incorporation can vary, which is in accordance with the absence of increase of tensile strain for Particle 2 after the reaction. The density of calcite particles grown on the gold membrane varies across different regions, as shown in Supplementary Fig. S6. During dissolution this can lead to local variations in the concentration of the species involved in the dissolution, which can affect the specific reaction rate and influence the  $\text{Pb}^{2+}$  incorporation.

## Conclusions

BCDI was employed to study the dissolution of individual calcite crystals in the presence of  $\text{Pb}^{2+}$ . The BCDI reconstructed morphologies and strain maps revealed that the most active sites for dissolution are close to macrosteps, and regions of pronounced tensile strain on the crystal surface. This information can be used to predict and optimize chemical reactions, enhancing its efficiency, with potential use in important chemical reactions such as the geochemical transportation of  $\text{Pb}^{2+}$  in the environment. With its ability to visualize the 3D morphology and strain of individual crystals before, during, and after chemical processes, BCDI is a very powerful tool that can be used to locate active sites in a chemical process. Importantly, we directly observe that dissolution of calcite in  $\text{Pb}^{2+}$ -containing solutions leads to significant changes in the 3D strain state of individual calcite particles.

This work establishes a methodological protocol for studying calcite particles before and after a dissolution reaction, tracking strain changes in both states, which can be extended to other chemical systems. BCDI provides unique insights into the 3D strain distribution and internal lattice distortions of individual particles, complementing other imaging and scattering techniques. While SEM offers high-resolution imaging of surface morphology and XR provides nanoscale interfacial information, BCDI adds a volumetric perspective, enabling the visualization of internal strain fields that influence reactivity. Together, these techniques provide a comprehensive approach for studying mineral dissolution. While our results suggest a connection between lattice strain and calcite reactivity, the limited dataset (two particles, two snapshots, no Pb-free control) prevents definitive conclusions about causation. Future studies with larger datasets, additional reaction time steps, and time-resolved measurements will be necessary to establish a more quantitative description of the strain–reactivity relationship. These challenges can be addressed with the recent advancements in 4th-generation synchrotron sources, which provide a significantly higher coherent X-ray flux, dramatically reducing measurement times and enabling the analysis of a larger number of particles.

## Methods

### Calcite synthesis

The synthesis of calcite was based on the ammonium carbonate diffusion approach, modified from previous works<sup>20–22</sup>, and published elsewhere<sup>23</sup>. Calcite was synthesized on a gold thin film containing hydroxyl-terminated self-assembled monolayers (SAMs). For the functionalization, the substrate was immersed in a 1 mM 11-mercapto-1-undecanol solution in ethanol at ambient conditions overnight in the dark. After rinsing with ethanol, the membrane was used as a substrate for the calcite synthesis, which consisted in placing ammonium bicarbonate powder in a petri dish in a ~2 L vessel. A drop of a 15 mM calcium chloride solution is deposited on the SAM functionalized substrate, which was left upside down above the ammonium carbonate. After 20 min of reaction, the vessel was open, and the substrate was rinsed with ethanol and dried.

### Scanning electron microscopy (SEM) and Energy dispersive X-ray (EDX)

The imaging/mapping were done using either a Zeiss Gemini or Thermo Scientific SEM models operating at 5–15 kV for SEM imaging and at 15 kV in fluorescence mode for EDX measurements. The SEM images of the same particles before and after dissolution reactions were collected by placing a drop of the reactant solution on the top of the membrane, waiting certain times for the reaction occurrence, drying it out using a wipe and putting the membrane under vacuum to guarantee that there is no remaining solution on the membrane surface. We were able to track the same particles by locating them on the membrane noting the 2-dimensional distances from the terminations of the membrane.

### X-ray reflectivity (XR)

XR measurements were performed at 33-ID-D beamline at Advanced Photon Source (APS), Argonne National Laboratory. The experiment was done in a specular geometry, using an X-ray beam energy of 18 keV, which was focused by a Kirkpatrick–Baez (KB) mirror. Crystal truncation rod (CTR) data were collected as a function of momentum transfer  $Q = \frac{4\pi \sin(2\theta/2)}{\lambda} = 2\pi L/d$ , where  $2\theta$  is the Bragg angle,  $\lambda$  is the wavelength of the X-rays (0.6888 Å), L is the Bragg index of the (104) calcite Bragg reflection, and d is the corresponding d spacing (3.035 Å). Datasets for pristine and  $\text{Pb}^{2+}$  reaction samples were collected in the 0.44–6.84 Å<sup>−1</sup> Q range.

All the solutions used during the experiment were prepared using deionized water (resistivity = 18.2 MΩ·cm). Calcite saturated solution (CSS) was prepared by dispersing calcite powder in deionized water and keeping it in a shaker table for 1–2 months, as described in our previous work<sup>23</sup>. Prior to use, the CSS was filtered using a paper filter. The  $\text{Pb}^{2+}$  containing solution was prepared by using  $\text{Pb}(\text{NO}_3)_2$  as the precursor, with a  $\text{Pb}^{2+}$  concentration in the final solution of 50 mM, which was acidified to pH = 3.6 using hydrochloric acid (HCl). Commercial calcite single crystals were cleaved right before the experiment to expose (104) surfaces. The crystals were then rapidly mounted in an X-ray thin film cell, which was filled with CSS for the calcite pristine state measurement. For the CTR measurement of the reaction with  $\text{Pb}^{2+}$ , the same procedure was done, followed by the injection of the  $\text{Pb}^{2+}$  solution. The CTR measurement was started after 15 min of the solution injection. The solution was maintained static inside the cell, and we measured three sets of CTR measurements, each of them taking ~15 min.

### Bragg Coherent Diffraction Imaging (BCDI)

The experiment was performed at 34-ID-C beamline at APS. A 10 keV coherent monochromatic beam was focused down to  $2 \times 2 \mu\text{m}^2$  using a pair of KB mirrors. The sequence of coherent diffraction patterns for the calcite (104) reflection (Bragg angle = 23.6°) was recorded in a Medipix detector (512 × 512 pixels, 55 × 55  $\mu\text{m}^2$ ). The sample to detector distance was the longest possible for this beamline, 2 m. The membrane containing the calcite crystals was mounted on a kinematic sample holder, which was placed on the sample stage of the beamline. The rocking curve of the (104)

Bragg peak was collected by using angular steps of 0.005° in either 40 or 60 points, with 15 or 30 s of exposure time, depending on the particle. The dissolution reaction was done with a pH = 3.7 solution (water acidified with HCl) containing 5 mM of lead nitrate ( $\text{Pb}(\text{NO}_3)_2$ ). A drop of ~100  $\mu\text{L}$  of this solution was placed on the top of the substrate, and left to react for 10 min. The substrate was then dried with a wipe and a laboratory air blower. BCDI measurements were done before (pristine state), and after the reaction. The 10 min timeframe for the dissolution reaction was chosen to minimize the risk of particle detachment from the substrate, which could occur during drying procedures involving the use of absorbent paper to remove excess solution if multiple intermediate timeframes were studied.

### Phase retrieval and strain calculation

The phase retrieval procedure started with 20 iterations of error reduction (ER) algorithm, followed by 180 iterations of hybrid input-output (HIO), where 620 iterations were used, ending with ER. The reconstruction was performed using the guided approach<sup>35</sup>, using 5 populations and 5 generations. The support was generated using the shrink-wrap approach. The strain was calculated as the gradient along the [104] direction of the projected displacement field. For the histogram plot of the surface of Particle 2 (pristine) shown in Fig. 4, we deleted 3 pixels that were very strained. All the histograms have been normalized and plotted as “Normalized counts”, defined as:

$$\text{Normalized counts} = \frac{\text{Number of counts in each bin}}{\text{Total number of counts} \times \text{bin size}}$$

The original number of counts for the plots shown in Fig. 4 are described in Table S3. The reconstructions were plotted in 3D as isosurfaces and 2D cross-sections of the image amplitude, phase, and strain using the software Paraview<sup>36</sup>.

### Data availability

The data presented in this paper and the Supplementary Information are archived at <https://doi.org/10.18126/zv82-ya03>.

Received: 18 June 2025; Accepted: 13 October 2025;

Published online: 28 November 2025

### References

1. Meldrum, F. C. Calcium carbonate in biomineralisation and biomimetic chemistry. *Int. Mater. Rev.* **48**, 187–224 (2003).
2. Wierzba, S., Makuchowska-Fryc, J., Klos, A., Ziembik, Z. & Ochedzan-Siodlak, W. Role of calcium carbonate in the process of heavy metal biosorption from solutions: synergy of metal removal mechanisms. *Sci. Rep.* **12**, 17668 (2022).
3. Abdilla, B., Lee, S. S., Fenter, P. & Sturchio, N. C. Dynamic inhibition of calcite dissolution in flowing acidic  $\text{Pb}^{2+}$  solutions. *Environ. Sci. Technol.* **58**, 7133–7143 (2024).
4. Morse, J. W. & Arvidson, R. S. The dissolution kinetics of major sedimentary carbonate minerals. *Earth Sci. Rev.* **58**, 51–84 (2002).
5. Renforth, P. & Henderson, G. Assessing ocean alkalinity for carbon sequestration. *Rev. Geophys.* **55**, 636–674 (2017).
6. Ai, Q., Bonagiri, L. K. S., Payam, A. F., Aluru, N. R. & Zhang, Y. J. Toward Quantitative Interpretation of 3D Atomic Force Microscopy at Solid-Liquid Interfaces. *J. Phys. Chem. C* **129**, 5273–5286 (2025).
7. Abdilla, B., Lee, S. S., Fenter, P. & Sturchio, N. C. Dynamic surface incorporation of  $\text{Pb}^{2+}$  ions at the actively dissolving calcite (104) surface. *Environ. Sci. Technol.* **58**, 16525–16534 (2024).
8. Hillner, P. E., Gratz, A. J., Manne, S. & Hansma, P. K. Atomic-scale imaging of calcite growth and dissolution in real-time. *Geology* **20**, 359–362 (1992).
9. Fenter, P. et al. Surface speciation of calcite observed in situ by high-resolution X-ray reflectivity. *Geochim. Cosmochim. Ac.* **64**, 1221–1228 (2000).
10. Miyata, K. et al. High-speed three-dimensional scanning force microscopy visualization of subnanoscale hydration structures on dissolving calcite step edges. *Nano Lett.* **24**, 10842–10849 (2024).
11. Arvidson, R. S. et al. Magnesium inhibition of calcite dissolution kinetics. *Geochim. Cosmochim. Ac.* **70**, 583–594 (2006).
12. Chada, V. G. R., Hausner, D. B., Strongin, D. R., Rouff, A. A. & Reeder, R. J. Divalent Cd and Pb uptake on calcite {1014} cleavage faces: An XPS and AFM study. *J. Colloid. Interf. Sci.* **288**, 350–360 (2005).
13. Chiarello, R. P. et al. Otavite-calcite solid-solution formation at the calcite-water interface studied in situ by synchrotron X-ray scattering. *Geochim. Cosmochim. Ac.* **61**, 1467–1474 (1997).
14. Godelitsas, A., Astilleros, J. M., Hallam, K., Harissopoulos, S. & Putnis, A. Interaction of calcium carbonates with lead in aqueous solutions. *Environ. Sci. Technol.* **37**, 3351–3360 (2003).
15. Callagon, E., Fenter, P., Nagy, K. L. & Sturchio, N. C. Incorporation of Pb at the calcite (104)-water interface. *Environ. Sci. Technol.* **48**, 9263–9269 (2014).
16. Kim, J. J. et al. Carbonate coprecipitation for Cd and Zn treatment and evaluation of heavy metal stability under acidic conditions. *Environ. Sci. Technol.* **8**, 3104–3113 (2023).
17. Yuan, K. et al. Pb-Calcite interactions under far-from-equilibrium conditions: formation of micropyramids and pseudomorphic growth of cerussite. *J. Phys. Chem. C* **122**, 2238–2247 (2018).
18. Yuan, K. et al. Mapping three-dimensional dissolution rates of calcite microcrystals: effects of surface curvature and dissolved metal ions. *ACS Earth Space Chem.* **3**, 833–843 (2019).
19. Abdilla, B. et al. Emergent behavior at the calcite-water interface during reactive transport in a simple microfluidic channel. *ACS Earth Space Chem.* **6**, 861–870 (2022).
20. Clark, J. N. et al. Three-dimensional imaging of dislocation propagation during crystal growth and dissolution. *Nat. Mater.* **14**, 780–785 (2015).
21. Ihli, J. et al. Strain-relief by single dislocation loops in calcite crystals grown on self-assembled monolayers. *Nat. Commun.* **7**, 11878 (2016).
22. Ihli, J. et al. Visualization of the effect of additives on the nanostructures of individual bio-inspired calcite crystals. *Chem. Sci.* **10**, 1176–1185 (2019).
23. Suzana, A. F. et al. Visualizing the internal nanocrystallinity of calcite due to nonclassical crystallization by 3D coherent x-ray diffraction imaging. *Adv. Mater.* **36**, 2310672 (2024).
24. Miao, J. & Sayre, D. On possible extensions of X-ray crystallography through diffraction-pattern oversampling. *Acta Crystallogr. A* **56**, 596–605 (2000).
25. Robinson, I. Nanoparticle Structure by Coherent X-ray Diffraction. *J. Phys. Soc. Jpn.* **82**, 021012 (2013).
26. Fenter, P. A. X-ray reflectivity as a probe of mineral-fluid interfaces: a user guide. *Rev. Mineral. Geochem.* **49**, 149–220 (2002).
27. Ihli, J., Bots, P., Kulak, A., Benning, L. G. & Meldrum, F. C. Elucidating mechanisms of diffusion-based calcium carbonate synthesis leads to controlled mesocrystal formation. *Adv. Funct. Mater.* **23**, 1965–1973 (2013).
28. Rodriguez-Blanco, J. D., Shaw, S. & Benning, L. G. The kinetics and mechanisms of amorphous calcium carbonate (ACO) crystallization to calcite, via vaterite. *Nanoscale* **3**, 265–271 (2011).
29. Radha, A. V., Forbes, T. Z., Killian, C. E., Gilbert, P. U. P. A. & Navrotksy, A. Transformation and crystallization energetics of synthetic and biogenic amorphous calcium carbonate. *Proc. Natl. Acad. Sci. USA* **107**, 16438–16443 (2010).
30. Han, Y. S., Hadiko, G., Fuji, M. & Takahashi, M. Effect of flow rate and  $\text{CO}_2$  content on the phase and morphology of  $\text{CaCO}_3$  prepared by bubbling method. *J. Cryst. Growth* **276**, 541–548 (2005).
31. Lee, J. R. I. et al. Structural development of mercaptophenol self-assembled monolayers and the overlying mineral phase during templated  $\text{CaCO}_3$  crystallization from a transient amorphous film. *J. Am. Chem. Soc.* **129**, 10370–10381 (2007).

32. Han, T. Y. J. & Aizenberg, J. Calcium carbonate storage in amorphous form and its template-induced crystallization. *Chem. Mater.* **20**, 1064–1068 (2008).
33. Schott, J. et al. Dissolution kinetics of strained calcite. *Geochim. Cosmochim. Ac.* **53**, 373–382 (1989).
34. Macinnis, I. N. & Brantley, S. L. The role of dislocations and surface-morphology in calcite dissolution. *Geochim. Cosmochim. Ac.* **56**, 1113–1126 (1992).
35. Chen, C. C., Miao, J., Wang, C. W. & Lee, T. K. Application of optimization technique to noncrystalline x-ray diffraction microscopy: Guided hybrid input-output method. *Phys. Rev. B* **76**, 064113 (2007).
36. Ahrens, J., Geveci, B., Law, C. *The Visualization Handbook* (Elsevier, Oxford, 2005).
37. Suzana, A. F. et al. Structure of a seeded palladium nanoparticle and its dynamics during the hydride phase transformation. *Commun. Chem.* **4**, 64 (2021).

## Acknowledgements

This research was supported by the U.S. Department of Energy, Office of Science, Office of Basic Energy Sciences, Geosciences program (FWP 57814) under Contract DE-AC02-06CH11357 to UChicago Argonne, LLC as operator of Argonne National Laboratory. The BCDI measurement was performed at 34-ID-C beamline at the Advanced Photon Source (APS), Argonne National Laboratory, beamtime award <https://doi.org/10.46936/APS-18392/60011389> and <https://doi.org/10.46936/APS-182573/60010866>. The CTR measurements were performed at the beamline 33-ID-D, APS, beamtime award <https://doi.org/10.46936/APS-180194/60009636>. This work used resources of the Advanced Photon Source, a U.S. DOE Office of Science User Facility operated for the DOE Office of Science by Argonne National Laboratory under Contract No. DE-AC02-06CH11357. ICA acknowledges financial support from the Spanish Agencia Estatal de Investigación, through Project No. PID2020-115159GBI00/AEI/10.13039/501100011033 and Aragones Project No. RASMIA E12-23R cofunded by Fondo Social Europeo of the European Union FEDER (ES).

## Author contributions

A.F.S., S.S.L., I.C.A., W.C., R.H., and P.F. performed the data collection. A.F.S. worked on the data analysis. A.F.S., S.S.L., I.C.A., and P.F.

contributed to the data interpretation. A.F.S. designed the main structure of the manuscript. All authors contributed to writing the manuscript.

## Competing interests

The authors declare no competing interests.

## Additional information

**Supplementary information** The online version contains supplementary material available at <https://doi.org/10.1038/s43246-025-00992-z>.

**Correspondence** and requests for materials should be addressed to Ana F. Suzana.

**Peer review information** *Communications Materials* thanks Xianping Liu and Dmitry Karpov for their contribution to the peer review of this work. A peer review file is available.

**Reprints and permissions information** is available at <http://www.nature.com/reprints>

**Publisher's note** Springer Nature remains neutral with regard to jurisdictional claims in published maps and institutional affiliations.

**Open Access** This article is licensed under a Creative Commons Attribution 4.0 International License, which permits use, sharing, adaptation, distribution and reproduction in any medium or format, as long as you give appropriate credit to the original author(s) and the source, provide a link to the Creative Commons licence, and indicate if changes were made. The images or other third party material in this article are included in the article's Creative Commons licence, unless indicated otherwise in a credit line to the material. If material is not included in the article's Creative Commons licence and your intended use is not permitted by statutory regulation or exceeds the permitted use, you will need to obtain permission directly from the copyright holder. To view a copy of this licence, visit <http://creativecommons.org/licenses/by/4.0/>.

© UChicago Argonne, LLC, Operator of Argonne National Laboratory 2025